

# Comparison of Multi-Parallel Slit and Knife-Edge Slit Prompt Gamma Cameras in the context of hadrontherapy verification

Brent F. B. Huisman<sup>1,2</sup>, É. Testa<sup>2</sup>, and D. Sarrut<sup>1</sup>

<sup>1</sup> CREATIS, Université de Lyon; CNRS UMR5220; INSERM U1206; INSA-Lyon;  
Université Lyon 1; Centre Léon Bérard, Lyon, France

<sup>2</sup> IPNL, Université de Lyon; CNRS/IN2P3 UMR5822; Université Lyon 1 Lyon, France  
E-mail: brent.huisman@cern.ch

June 22, 2018

## Abstract

*Purpose:*

*Materials and Methods:*

*Results:*

*Conclusion:*

## Contents

<b>1</b>	<b>Introduction</b>	<b>2</b>
<b>2</b>	<b>Materials and Methods</b>	<b>2</b>
2.1	Features of PG profiles . . . . .	2
2.2	Geometrical considerations . . . . .	3
2.2.1	Parameters . . . . .	3
2.2.2	Definitions and figures of merit . . . . .	4
2.3	Monte Carlo simulations . . . . .	4
2.3.1	Simulation tool . . . . .	5
2.3.2	PG camera modeling . . . . .	6
2.3.3	Background estimation . . . . .	6
2.3.4	Fall-off position estimation procedure . . . . .	8
<b>3</b>	<b>Results</b>	<b>8</b>
3.1	Geometrical considerations . . . . .	8
3.2	Monte Carlo simulations . . . . .	9
3.2.1	Geometrical considerations verification . . . . .	9
3.3	Clinical case study . . . . .	10
<b>4</b>	<b>Discussion</b>	<b>11</b>
<b>5</b>	<b>Conclusion</b>	<b>11</b>
<b>6</b>	<b>Acknowledgements</b>	<b>11</b>
<b>A</b>	<b>Fall-off position estimation procedure</b>	<b>12</b>
<b>B</b>	<b>Verification of the cameras</b>	<b>12</b>

# 1 Introduction

**State of the art** At the moment, two papers have proposed a comparison of MPS-KES cameras:

- Smeets 2016 Fontiers in Oncology: experimental comparison with a non-optimized CLaRyS MPS camera (some technical constraints prevented the authors to use the “optimal CLaRyS design”)
- Lin 2017 Radiation Physics and Chemistry : MC comparison with the MPS Korean design whose optimization procedure is actually questionable

In overall, the camera configurations present many parameters, namely geometrical parameters and event selections (especially energy deposition selection). Therefore, in principle, some theoretical expectations are required to set relevant parameters and to allow for a fair comparison of the two types of collimators. Although the aforementioned studies may give the impression to provide a fair comparison (use of the same absorbers, same beam-collimator and collimator-absorber distance in the case of Lin 2017), they do not provide a thorough justification of their sets of parameters. Surprisingly, some parameters are even not the same between the two camera types. While it can be understood in Smeets 2016 due to experimental constraints, it is more questionable Lin 2017 (different energy deposition selection).

**Objectives** The objectives of the present paper are the following:

- Estimate the MPS and KES detection efficiencies and spatial resolution from geometrical considerations
  - Draw some conclusions about the intrinsic features of MPS and KES collimators:
  - Estimate various MPS and KES performances
    - \* In Smeets 2016 and Lin 2017: the KES/MPS detection efficiency ratio is 1.6 for Smeets 2016 and 5.3 for Lin 2017 (assuming the use of the same energy window)  $\Rightarrow$  these comparisons were unfair...
    - \* "Official" MPS and KES prototypes with identical absorbers
- MC simulation: geometrical considerations verification and prototype direct comparison

## 2 Materials and Methods

### 2.1 Features of PG profiles

Figure 1 defines the 3 parameters of a typical PG profile measured with a collimated camera in the falloff region and in the case of a homogeneous target irradiation.

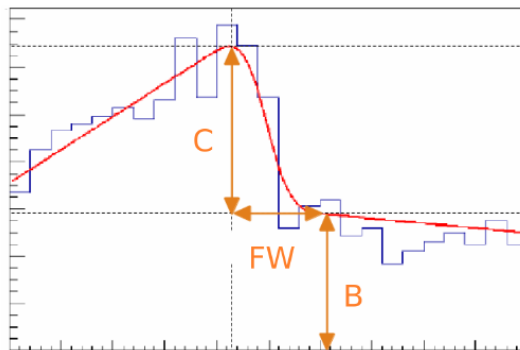


Figure 1: PG profile parameters.

The 3 parameters are the following:

- the contrast  $C$  corresponding to the falloff amplitude,

- the background level  $B$ ,
- and the falloff  $FW$  width related to the camera spatial resolution (Note that the PG emission profile has an intrinsic width of a few millimeters. In practice the width of PG emission profiles measured by the collimated camera prototypes is dominated by the camera resolution of the order of 20 mm).

As expected, these 3 parameters have very different impacts on the falloff retrieval precision ( $FRP$ ). As mentioned in [Roellinghoff MPB 2014],  $FRP$  is mainly determined by the contrast-to-noise ratio of the profile. The detailed study of the influence of  $C$ ,  $B$  et  $FW$  on  $FRP$  has shown that [Roellinghoff PhD thesis 2014]:

- $FRP \propto \frac{\sqrt{B}}{C}$
- The influence of  $FW$  is negligible

As a consequence, the optimization of the collimated cameras is actually a compromise between  $FRP$  and spatial resolution  $FW$ . In principle, collimator slits have to be as large as possible to increase detection efficiency and minimize  $FRP$ . However, a “reasonable” spatial resolution has obviously to be defined and it has been set in the range of  $\sim 1$  to 2 cm depending on the collimator types. Moreover, this spatial resolution can play a major role in clinical conditions since the beam might cross highly heterogeneous regions. More specifically, Priegnitz et al. have shown that the KES prototype is not able to detect the filling of a cavity located 5 mm upstream to the Bragg peak position [Priegnitz PMB 2015].

## 2.2 Geometrical considerations

	Multi-parallel slit	Knife-edge
Effective slit width ( $s_e$ )	$s$	$\left(s + \frac{\ln(2)}{\mu \tan(\alpha)}\right)$
Det. unit FOV	$s \left(1 + \frac{d_1}{D}\right)$	$s_e \left(1 + \frac{d_1}{d_2}\right)$
Lin. collection efficiency	$\frac{Hs}{4\pi LD} (1 - f)$	$\frac{Hs_e}{4\pi Ld_2} \left(1 + x^2/d_2^2\right)^{-3/2}$
Effective thickness ( $T_e$ )	$Df$	$T$

Figure 2: MPS and KES detection efficiencies and spatial resolution from geometrical considerations. The parameters of the cameras are defined in figure 3.

- Rationale: geometrical considerations should provide good predictions of collimated camera performances while providing a good understanding of the intrinsic features of the 2 types of collimators.
- Estimate the MPS and KES performances in Smeets 2016 and Lin 2017: the KES/MPS detection efficiency ratio is 1.6 for Smeets 2016 and 5.3 for Lin 2017 (assuming the use of the same energy window)  $\Rightarrow$  these comparisons were unfair. . .

### 2.2.1 Parameters

- Geometrical parameters (Figure 3)
- Energy and TOF selections

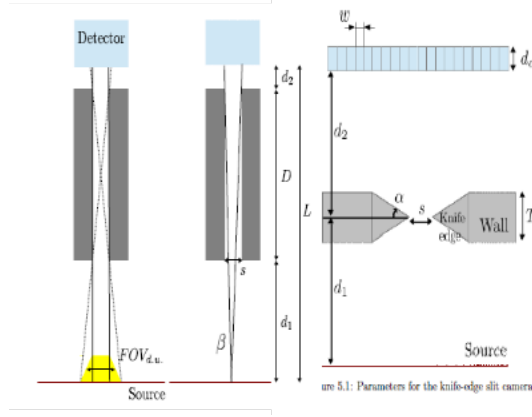


Figure 3: Schemes of MPS and KES cameras.

### 2.2.2 Definitions and figures of merit

#### Definitions

- Detector unit field of view: This is the part of the source that can be “seen” through a single camera unit: a single slit for the MPS (naturally associated to a single detector unit) and a single detector unit for KES. The probability of a photon emitted at a given point along a linear source (perpendicular to the slit plane) to reach this detector unit can be described as a trapezoid: the part that can be seen from every points on the detector unit and the penumbra.
- Collection efficiency: The probability of a photon emitted at a point facing a slit (in the middle part of the trapezoid) to reach the detector is described by the solid angle that the point sees of the detector.
- Linear collection efficiency: collection efficiency divided by the pitch that corresponds to the collection efficiency of the camera per unit of length
- Effective Slit Opening (especially for KES): At the particle energies that occur in prompt-gamma imaging, a non-negligible amount of particles will cross the collimator slit edges. This effect can be approximated by introducing an effective slit opening that can be used in the evaluation of the field of view and the efficiency in place of the geometrical slit opening.
- Spatial resolution: PSF width. In the context of PG detection, the gamma source can be considered at first order as a linear source. Hence one can estimate the spatial resolution of the collimated camera from the derivative of the PG profile that has a gaussian-like shape. The width of the derivative can be defined as the spatial resolution of the collimated cameras in the context of PG detection.

#### Figures of merit

- Linear collection efficiency ( $LCE$ )
- Spatial resolution ( $SR$ )
- Falloff retrieval precision ( $FRP$ )

### 2.3 Monte Carlo simulations

- Geometrical considerations verification: Fair comparison of the two types of collimators with MC simulations. What does it mean?

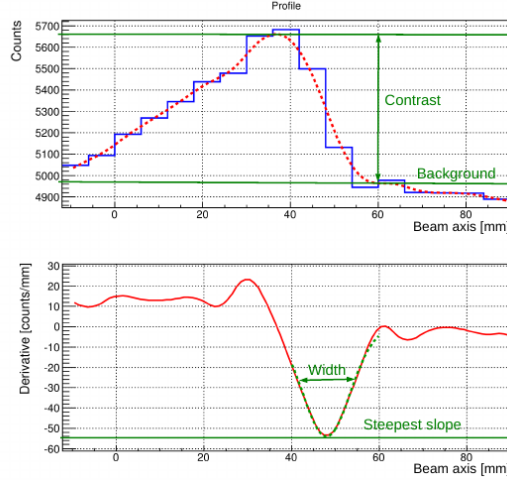


Figure 4: Example of PG profile falloff width (FW) estimate with the first derivative of the PG profile (Figure 4.15 of Frauke’s manuscript).

- Use of same absorbers (the LYSO absorber of the KES prototype that we can consider as the reference), the same energy selection which was not the case in Lin 2017 and the same TOF selection (no TOF)
- Then a discussion of the results in the light of the geometrical considerations
- Note: the KES background level can be obtained from Figure 18 in Perali 2014. Regarding the MPS background level I propose to use the same level as the one of KES for the following reasons: i) the background level in the MPS camera is derived in Pinto 2014 from measurements with large detectors by assuming that the background is proportional to the detector volume. If we apply the same approach, it is reasonable to use the same background levels since we use the same absorbers for MPS and KES. One can argue that the MPS and KES collimators are different. It is true and it is difficult to say whether the larger amount of material in the CLaRyS MPS collimator leads to a larger background with more neutron-induced gammas or a lower background due to a larger attenuation of these gammas. . . At first order the background levels should be similar and a first order estimate is sufficient for a paper that mainly aims at comparing the signal detection of the two cameras.
- Simulations of the two prototypes as they are published (results of the submitted paper with the “regular” cylindrical PMMA target of 15 cm diameter and 20 cm lenght).
  - $\Rightarrow$  Comparison of the two prototypes
  - Identification of the impact of energy ( $>1$  MeV vs 3-6 MeV selection for KES) and TOF selection (for MPS) although the latter has been already shown in Roellinghoff PMB 2014 with a large detector placed behind a single slit collimator
  - Note that the absorbers have different thicknesses

### 2.3.1 Simulation tool

Imaging paradigms such as PG detection are evaluated against experiments, and often also with Monte Carlo (MC) simulations (Golnik et al., 2014; Gueth et al., 2013; Janssen et al., 2014; Moteabbed et al., 2011; Robert et al., 2013). For rarely occurring processes such as PG simulation, convergence to the model of the truth to within acceptable statistical error can be slow. This paper presents an *in silico* study of the feasibility of the clinical relevance of PG FOP estimation using collimated cameras, and uses the vpgTLE variance reduction method described in Huisman et al. (2016). vpgTLE is a two stage process, where firstly a PG yield distribution image is estimated, which in the second stage is used as a PG source with which detectors can be investigated. Gate 7.2 (Sarrut et al., 2014) with Geant 4.10.02

and the QGSP\_BIC\_HP\_EMY physics list, commonly used for PG studies, are used in this analysis. Thanks to vpgTLE, simulations for about  $10^9$  protons (about  $6 \times 10^8$  photons) took 1-2 hours on a single core of an Intel(R) Core(TM) i7-3740QM.

### 2.3.2 PG camera modeling

Two PG detectors tailored to FOP verification (illustrated in fig. 5) were chosen:

- the CLaRyS multi-parallel-slit (MPS) camera, Case 1 (Pinto et al., 2014)  
This camera intends to measure the whole PG profile to control ion-ranges in the patient with a field of view (FoV) of 300 mm. It makes use of ToF selection to reduce the neutron background. In the optimization carried out by Pinto et al. (2014), parameters such as collimator pitch, axis-to-collimator and axis-to-detector were varied, and their impacts evaluated in terms of fall-off retrieval precision (FRP) and spatial resolution (sharpness of the fall-off region). Here, configuration 1 (with relaxed constraints on spatial resolution) was chosen for its optimal FRP performance. As was done by Pinto et al. (2014), the camera lengths (collimator and scintillator volume) are chosen *up to* 300 mm, such that the length is an integer multiple of the pitch size, with for the collimator a collimator-leaf-width extra, to ensure each pixel has a leaf on both sides. With the 8 mm pitch and 2.6 mm collimator-leaves, this results in a scintillator volume of length 296 mm and collimator length 298.6 mm.
- the IBA knife-edge (KES) camera (Perali et al., 2014; Sterpin et al., 2015)  
The purpose of this camera consists of verifying the BP position with a FoV of 100 mm. Richter et al. (2016) provides the first clinically obtained results. At this time, no other camera has been subjected to clinical tests, which is why we consider this prototype a benchmark.

Regarding background ToF selection, for the IBA C230 accelerator with a period of 10 ns, Pinto et al. (2014) chose a window of 4 ns around the PG maximum, based on experimental ToF spectra. This means that about 60% of the noise could be removed. For the KES prototype ToF is not used, leading to a higher background, as is evident when one compares the backgrounds as published in the two publications. A second difference is the energy selection window. The IBA group employ a 3-6 MeV window, whereas the CLaRyS collaboration produced their optimization with a 1-8 MeV window. We will compare each camera with their published properties, that is to say: a 1-8 MeV window and ToF for MPS and a 3-6 MeV window without ToF for KES.

Both PG camera prototypes have different photodetectors and different detector electronics. In this study, these differences are not implemented. Instead, the method as described in Gueth et al. (2013) was used to obtain the interaction point of an impinging photon. If the integrated energy deposited in a crystal lies in the acceptable energy and ToF window, the event is recorded. The position of the event in the crystal is considered as the energy weighed barycenter of all interactions in the crystal, plus a random value taken from a 5mm FWHM Gaussian to simulate the electronics and the detector resolution.

**Fair Comparison** Since we are using a simulation for the validation of the theoretical expressions in table 2, for the fairest comparison possible, we can equalize certain aspects which might cause one camera or the other to give favorable impression. In principle this comparison is not about absorption materials, acquisition electronics or PG selections, but PG collimator characteristics. So, for the validation of the expressions in table 2 and comparison on LCE, SR and FRP we set the absorber material of the MPS to that of the KES: LYSO. The energy and ToF selection windows are kept identical for both cameras, and are varied in order to study their impact on the figures of merit.

### 2.3.3 Background estimation

Background estimation in PG simulation is a difficult and largely unsolved issue (Huisman et al., 2016; Perali et al., 2014; Pinto et al., 2014; Sterpin et al., 2015). Simulations would ideally include beam nozzle and whole room modeling, but these are habitually omitted. ToF selection techniques can improve the signal-to-noise ratio (SNR) (Roellinghoff et al., 2014; Testa et al., 2008), but then depend on the proper simulation of the beam accelerator time structure. As noted in Huisman et al. (2016), no validation for background in PG simulations has been performed at this time. In this study, the stable time structure of current generation cyclotrons was assumed, in which the neutron background is largely constant.

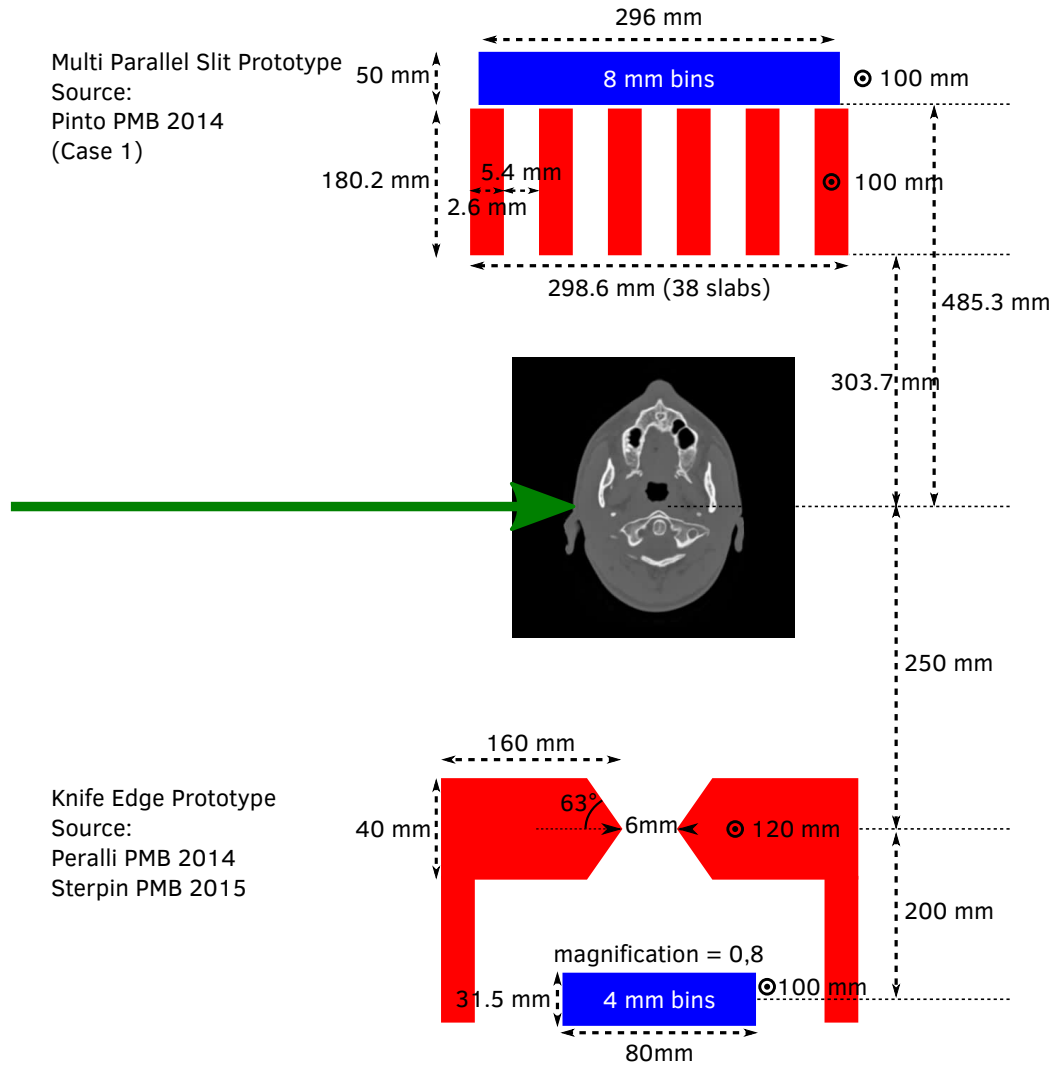


Figure 5: Schematic presentation of the two PG cameras considered in this study. The green arrow represents the proton beam. In red the collimation elements and in blue detection elements. The dimensions were taken from Pinto et al. (2014) and Peralli et al. (2014); Sterpin et al. (2015). Note that the two cameras have an identical detector height ( $\odot$  symbol), the two cameras were positioned at an identical location above the head during all simulations, and that here they are not drawn to scale.

Estimates of background counts in the detector are taken from Perali et al. (2014); Pinto et al. (2014), which are both based on measured data:

- MPS: Pinto et al. (2014) fig. 9:  $1 \cdot 10^3 \pm 1 \cdot 10^2$  per  $4 \cdot 10^9$  primary protons per 8 mm bin  
Converted to per primary proton:  $2.5 \cdot 10^{-7} \pm 0.25 \cdot 10^{-7}$
- KES: Perali et al. (2014) fig. 11:  $5 \cdot 10^{-7} \pm 0.5 \cdot 10^{-7}$  per primary proton per 4 mm bin

Per unit of bin length, the background yield of the MPS with ToF is therefore 4 times as low as the background seen with the KES. In the context of the fair comparison, for the KES camera the background with ToF can be obtained by multiplying the background with the same  $\frac{4ns}{10ns} = 0.4$  fraction as with the MPS (

### 2.3.4 Fall-off position estimation procedure

From a clinical perspective, the range estimate could be more interesting than FOP, because it can distinguish simple offset errors from patient morphological change. While the MPS camera was conceived for whole range PG profile detection, the KES camera FoV was chosen for BP region PG detection only. To make the comparison fair, only the FOP could be considered. Multiple approaches to extracting a FOP from the line profile have been proposed (Gueth et al., 2013; Janssen et al., 2014; Roellinghoff et al., 2014; Smeets et al., 2012; Sterpin et al., 2015). In preparatory work, a number of the proposed procedures were investigated. Significant sensitivity to free parameters on the final FOP estimates were seen. In summary, the FOP estimate depends greatly on the procedure, and often on having yields uncommon on the spot-level in clinical TPs, and also on an absence of unavoidable inhomogeneities.

Therefore the fitting method was not chosen as a topic for study in this paper. Instead, a simple method that works on most the data available to the authors was used: first a smoothed and interpolated spline function is fitted against the detected PG data points, after which a baseline and (distal) peak position are determined. The intersection of the spline with the half-height of the peak above the baseline is then taken as the FOP. A more detailed description of the procedure may be found in appendix A.

## 3 Results

### 3.1 Geometrical considerations

For the validation of the theoretical expressions in table 2, the two cameras are equalized by settings the absorber material to LYSO in the MPS camera and the PG energy selection window to 1-8 MeV.

- Formulas of the the MPS and KES detection efficiencies and spatial resolution from geometrical considerations (figure 2)
  - Draw some conclusions about the intrinsic features of MPS and KES collimators knowing that the falloff retrieval precision (FRP)
    - \* Efficiency: same efficiency with the same  $s, L, H$ ,  $d_2(\text{KES}) = D(\text{MPS})$ ,  $d_2(\text{MPS}) = 0$  (no space between collimator and absorber in MPS) and  $f \rightarrow 0$  (perfect collimator). In practice,  $f \neq 0$  ( $f = 0.4$  in the CLaRyS MPS camera) so that the KES camera has a slightly larger efficiency than the MPS camera with the aforementioned geometrical conditions. It is worth noting that the KES detection efficiency is not constant over the FOV.
    - \* Spatial resolution: same resolution with the same geometrical conditions and perfect collimators. In practice, MPS transparency can be neglected in the CLaRyS prototype ( $D = 180$  mm) but not the KES transparency so that the KES camera has a slightly poorer spatial resolution than the one of the MPS camera (still with the aforementioned geometrical conditions).
  - Estimate the MPS and KES performances in Smeets 2016 and Lin 2017: the KES/MPS detection efficiency ratio is 1.6 for Smeets 2016 and 5.3 for Lin 2017 (assuming the use of the same energy window)  $\Rightarrow$  these comparisons were unfair...

( Roellinghoff et al. (2014) shows impact of TOF )



Smeets 2016

	Geometrical calculations	
	MPS	KES
d1 (mm)	300	300
D (mm)	200	
d2 (mm)	300	300
L (mm)	800	600
s (mm)	2	6
septa (mm)	2	
f	0,5	
Effective thickness (mm)	100	40
Det. Unit FOV (mm)	5	12
Lin. Coll. Eff (relative)	6,25E-006	3,33E-005
Falloff amplitude (4 mm bin)		
KES eff/ MPS eff	5,333333333	
* no KES transparency taken into account		
** Efficiency at the center of the camera		

(a) Smeets 2016 setup

(b) Lin's setup

Figure 6: MPS and KES comparisons in litterature.

## 3.2 Monte Carlo simulations

TODO: Estimate of the falloff width from the PG profile derivative (see Material and methods section).

### 3.2.1 Geometrical considerations verification

I think it would be better to show PG profiles with 1-8 MeV energy selection with no TOF selection. The advantage of these selections is that it allows us to show the impact of energy ( $>1$  MeV vs 3-6 MeV selection for KES) and TOF selection (for MPS) when we move to the prototypes configurations. We can put in the table of Figure 8 the result with the 3-6 MeV energy selection to show that the results do not depend on energy selection).

Figures 7 and 8.

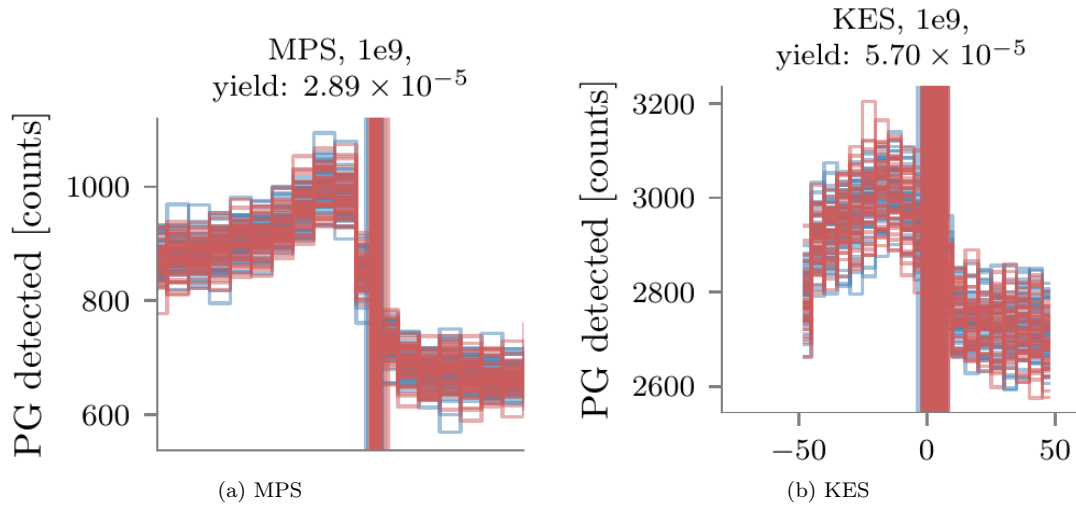


Figure 7: MPS and KES comparisons with the same absorber and the same energy (3-6 MeV) and TOF selection (no TOF selection). Sum the statistics of the various 1e9 PG profiles to get the smoothest profiles (we are interested in PG profile shapes). This will allow us to better estimate the falloff features, namely amplitude and width. Put the 2 PG profiles on a single figure?

	MPS	KES	Simulation results			
			NoTOF 3-6 MeV		TOF 1-8 MeV	
			MPS	KES	MPS	KES
d1 (mm)	304	250				
D (mm)	180					
d2 (mm)	0	200				
L (mm)	484	450				
s (mm)	5.4	6*				
septa (mm)						
f	0.325					
Effective thickness (mm)	58.5	40	72			
Det. Unit FOV (mm)	14.52	13.5				
Lin. Coll. Eff (relative)	4.18E-005	6.67E-005**				
Falloff amplitude (4 mm bin)			200	350	400	700
KES eff/ MPS eff	1.59341564		1.75		1.75	
* no KES transparency taken into account						
** Efficiency at the center of the camera						

Figure 8: MPS and KES comparisons with the same absorber, energy and TOF selection. The first columns of the table correspond to the geometrical calculations. It is interesting to show the results for the two energy selections but it would be nice to have only one TOF selection (no TOF).

### 3.3 Clinical case study

Performance under clinical conditions is the eventual purpose of these PG cameras, and therefore we here include the results of the clinical case study.. Since both cameras prototypes were optimized assuming their particular choice for absorber and energy selection window, here we chose to set

**PG profiles** Figure 9.

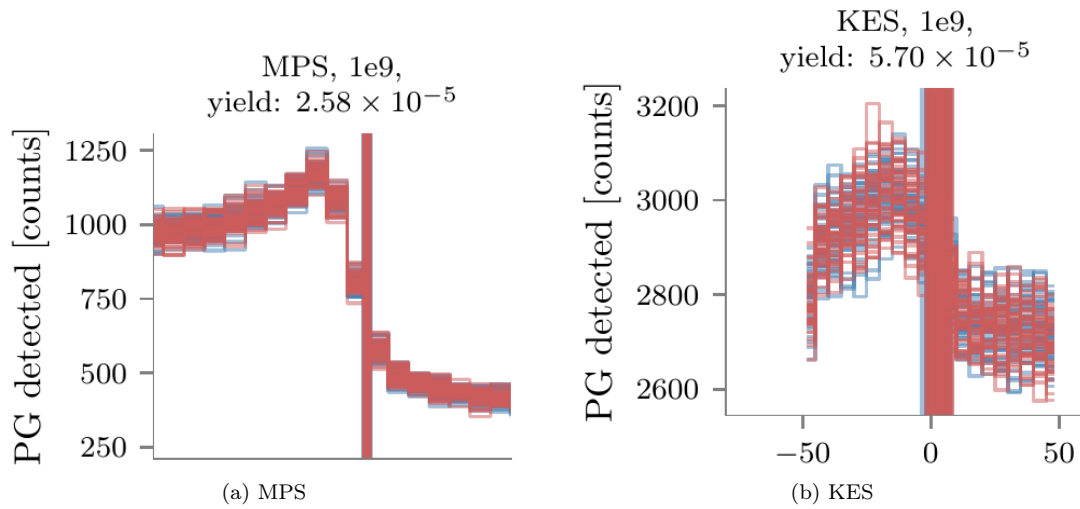


Figure 9: MPS and KES prototypes comparisons. MPS BGO absorber with 1-8 MeV energy selection and TOF selection. KES: LYSO absorber with 3-6 MeV and no TOF selection). Sum the statistics of the various 1e9 PG profiles to get the smoothest profiles (we are interested in PG profile shapes). This will allow us to better estimate the falloff features, namely amplitude and width. Put the 2 PG profiles on a single figure?

KES/MPS ratio  $\sim 400/350 \sim 0.9$ .

**FRP** Figure showing the falloff retrieval precision (FRP) (standard deviation of the falloff position distributions) for the 2 prototypes as a function of the number of incident protons ( $10^7$ ,  $10^8$ ,  $10^9$ ).

We do not have this figure yet. The figure in the spot grouping paper shows the mean and standard deviations on the falloff position differences for the 3 spots considered.

## 4 Discussion

## 5 Conclusion

## 6 Acknowledgements

This work was partly supported by SIRIC LYric Grant INCa-DGOS-4664, LABEX PRIMES (ANR-11-LABX-0063 / ANR-11-IDEX-0007) and Fondation ARC. The authors would like to thank Marie-Claude Biston, Thomas Baudier and Gloria Vilches-Freixas for their help finding the CT images and making the treatment plan. We also thank Erik Almhagen and Uppsala University Hospital, Sweden for the treatment plan data presented in this paper.

## A Fall-off position estimation procedure

1. The measured PG profile is smoothed and interpolated with a smoothing spline function:

$$\sum_{i=1}^n (y_i - \hat{f}(x_i))^2 + \lambda \int_{x_1}^{x_n} \hat{f}''(x)^2 dx \quad (1)$$

where  $y_i$  is the measured PG profile and  $x_i$  the associated x-coordinates,  $\hat{f}(x_i)$  the estimate smoothed spline function and  $\lambda$  a smoothing parameter that determines the penalty for deviating from measurement in exchange for smoothness (second order derivatives are close to zero on smooth functions).  $\lambda = 0$  produces a perfect spline fit to the data, while  $\lambda \gg 1$  produces a horizontal line. We found that  $\lambda = 2$  provided an acceptable trade-off between overfitting to noise and removing too many features, which tends to happen for low statistic measurements.

2. The obtained function is plotted for 1024  $x_j$ , an number that provided a sufficiently high resolution. Any  $f(x_j) < 0$  are set to 0.
3. The global maximum is found.
4. The baseline is set equal to the lowest 25% of bins.
5. From the distal end backwards, the first maximum is taken as the distal most peak position, if it is above the threshold of 30% of the difference between baseline and global maximum. If no such point is found, the global maximum is taken as the distal most maximum.
6. The fall-off amplitude (FOA) is set to the difference between the distal maximum and baseline:  $FOA = \max - \text{baseline}$ . The FOP is obtained by traversing the smoothed profile from the distal end towards the peak until  $y_j > \frac{1}{2}FOA$ .

The results of this procedure are illustrated in figure 10. Every PG profile was estimated 50 times, and so we obtained 50 estimates for the FOP. It is assumed that the FOPs follow a Gaussian distribution, so the mean of the 50 realizations gives the best FOP estimate and the sigma gives the precision of the ability to estimate the best FOP. Comparing the 50 FOP estimates obtained from the CT with the 50 estimates obtained from the RPCT simulations, gives 2500 possible shift estimates. Again, the distribution of shifts should be centered at the true shift, while the sigma indicates how likely it is that this true shift is detected under the current conditions.

## B Verification of the cameras

In Priegnitz et al. (2015) PG shifts due to beam energy shifts are studied for the KES camera: the *detectability* of the fall-off as function of the number of primaries. Here that simulation was recreated: a mono-energetic beam shoots into a waterbox at two energies. 50 realizations are generated with a 139 MeV beam energy, and 50 realizations with 144 MeV. At  $10^9$  primaries, the distributions are well separated with a shift of 8.3 mm (different from Priegnitz et al. (2015) because of the different material). In figure 13 in Perali et al. (2014) with  $10^9$  primaries a standard deviation of 1.5 mm is obtained, while here 1.21 and 1.14 mm were obtained. It is sufficient agreement to be confident of our setup and further results.

The KES prototype's sensitivity to accurate positioning with respect to the expected FOP was elaborated upon in Sterpin et al. (2015, Section IV.A.3): the detector response is, due to the KES collimator, not linear as with a parallel slit collimator. In this study, to make the comparison as fair as possible and avoid any bias, alignment on the FOP specific for each spot was ensured as follows: the intermediate PG source image of vpgTLE (equivalent to the PG emission) was projected on the beam axis, and then convolved with a Gaussian of  $\sigma = 8.5$  mm, which corresponds to the point spread function (PSF) with a FWHM of 20 mm used in Priegnitz et al. (2015) to approximate the detected profiles from the emitted profile. These profiles will be referred to as "PG + PSF" profiles. As a matter of fact, the MPS prototype has roughly the same PSF as the KES prototype so that "PG + PSF" fall-off position can be considered as the expected position for both cameras.

To verify the implementation of the MPS camera, the precision on the FOP, obtained with the procedure outlined in the previous paragraph, is compared to earlier results. In the caption of figure 9 in Pinto et al. (2014) it is stated that with  $10^8$  primaries a standard deviation of 1.3 mm is obtained for

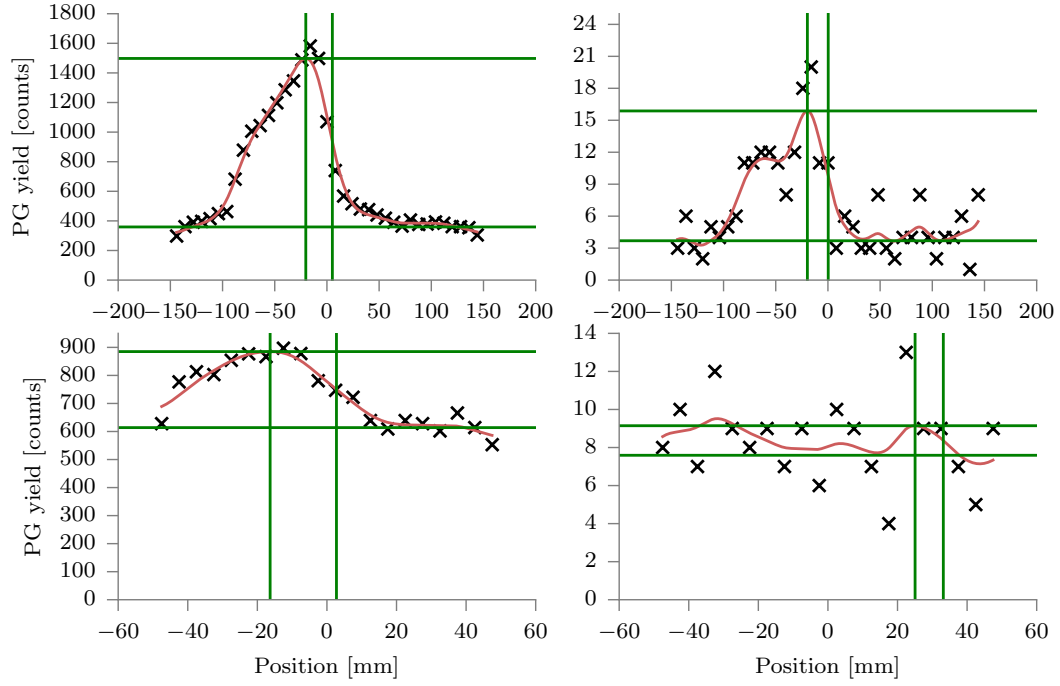


Figure 10: The top row demonstrates the fall-off determination procedure on the multi-parallel camera data; on the bottom row on knife-edge slit camera data. The left column is produced with a PG signal due to  $10^9$  primaries, while the right column was produced with  $10^7$  primary protons. In black crosses the measured PG counts are plotted. The smoothed data is shown in red. The green horizontal lines are drawn at the obtained distal maxima and baselines, while the vertical green lines shown the position of the distal maximum and the position of the fall-off. For the bottom-right plot, a history is visible where the procedure fails: the background induces an erroneous peak detection.

the detector design used here, which is about 20% different from the results obtained in this study: 1.63 and 1.54 mm.

## References

- Christian Golnik, Fernando Hueso-González, Andreas Müller, Peter Dendooven, Wolfgang Enghardt, Fine Fiedler, Thomas Kormoll, Katja Roemer, Johannes Petzoldt, Andreas Wagner, and Guntram Pausch. Range assessment in particle therapy based on prompt  $\gamma$ -ray timing measurements. *Physics in Medicine and Biology*, 59(18):5399–5422, sep 2014. ISSN 0031-9155. doi: 10.1088/0031-9155/59/18/5399. URL <http://stacks.iop.org/0031-9155/59/i=18/a=5399?key=crossref.5437fcd3059992135ec2113679c7dad6>.
- P Gueth, D Dauvergne, N Freud, J M Létang, C Ray, E Testa, and D Sarrut. Machine learning-based patient specific prompt-gamma dose monitoring in proton therapy. *Physics in medicine and biology*, 58(13):4563–77, jul 2013. ISSN 1361-6560. doi: 10.1088/0031-9155/58/13/4563. URL <http://www.ncbi.nlm.nih.gov/pubmed/23771015>.
- Brent F B Huisman, J M Létang, É Testa, and D Sarrut. Accelerated Prompt Gamma estimation for clinical Proton Therapy simulations. *Physics in Medicine and Biology*, 61:7725–7743, 2016. ISSN 0031-9155. doi: 10.1088/0031-9155/61/21/7725.
- F M F C Janssen, G Landry, P Cambraia Lopes, G Dedes, J Smeets, D R Schaart, K Parodi, and F Verhaegen. Factors influencing the accuracy of beam range estimation in proton therapy using prompt gamma emission. *Physics in medicine and biology*, 59(15):4427–41, aug 2014. ISSN 1361-6560. doi: 10.1088/0031-9155/59/15/4427. URL <http://www.ncbi.nlm.nih.gov/pubmed/25049223>.
- M Moteabbed, S España, and H Paganetti. Monte Carlo patient study on the comparison of prompt gamma and PET imaging for range verification in proton therapy. *Physics in medicine and biology*, 56(4):1063–82, feb 2011. ISSN 1361-6560. doi: 10.1088/0031-9155/56/4/012. URL <http://www.ncbi.nlm.nih.gov/pubmed/21263174>.
- I Perali, a Celani, L Bombelli, C Fiorini, F Camera, E Clementel, S Henrotin, G Janssens, D Prieels, F Roellinghoff, J Smeets, F Stichelbaut, and F Vander Stappen. Prompt gamma imaging of proton pencil beams at clinical dose rate. *Physics in Medicine and Biology*, 59(19):5849–5871, oct 2014. ISSN 0031-9155. doi: 10.1088/0031-9155/59/19/5849. URL <http://stacks.iop.org/0031-9155/59/i=19/a=5849?key=crossref.d1c598721e0b970b36f1c8a6ad1dd1a1>.
- M Pinto, D Dauvergne, N Freud, J Krimmer, J M Letang, C Ray, F Roellinghoff, and E Testa. Design optimisation of a TOF-based collimated camera prototype for online hadrontherapy monitoring. *Physics in medicine and biology*, 59(24):7653–7674, 2014. ISSN 1361-6560. doi: 10.1088/0031-9155/59/24/7653. URL <http://www.ncbi.nlm.nih.gov/pubmed/25415207>.
- M Priegnitz, S Helmbrecht, G Janssens, and I Perali. Measurement of prompt gamma profiles in inhomogeneous targets with a slit camera. *Physics in Medicine and Biology*, 4849:4849, 2015. ISSN 0031-9155. doi: 10.1088/0031-9155/60/12/4849. URL <http://dx.doi.org/10.1088/0031-9155/60/12/4849>.
- Christian Richter, Guntram Pausch, Steffen Barczyk, Marlen Priegnitz, Isabell Keitz, Julia Thiele, Julien Smeets, Francois Vander Stappen, Luca Bombelli, Carlo Fiorini, Lucian Hotoiu, Irene Perali, Damien Prieels, Wolfgang Enghardt, and Michael Baumann. First clinical application of a prompt gamma based in vivo proton range verification system. *Radiotherapy and Oncology*, 118(2):232–237, 2016. ISSN 18790887. doi: 10.1016/j.radonc.2016.01.004. URL <http://linkinghub.elsevier.com/retrieve/pii/S0167814016000074>.
- C Robert, G Dedes, G Battistoni, T T Böhlen, I Buvat, F Cerutti, M P W Chin, a Ferrari, P Gueth, C Kurz, L Lestand, a Mairani, G Montarou, R Nicolini, P G Ortega, K Parodi, Y Prezado, P R Sala, D Sarrut, and E Testa. Distributions of secondary particles in proton and carbon-ion therapy: a comparison between GATE/Geant4 and FLUKA Monte Carlo codes. *Physics in medicine and biology*, 58(9):2879–99, may 2013. ISSN 1361-6560. doi: 10.1088/0031-9155/58/9/2879. URL <http://www.ncbi.nlm.nih.gov/pubmed/23571094>.
- F Roellinghoff, a Benilov, D Dauvergne, G Dedes, N Freud, G Janssens, J Krimmer, J M Létang, M Pinto, D Prieels, C Ray, J Smeets, F Stichelbaut, and E Testa. Real-time proton beam range

monitoring by means of prompt-gamma detection with a collimated camera. *Physics in medicine and biology*, 59(5):1327–38, 2014. ISSN 1361-6560. doi: 10.1088/0031-9155/59/5/1327. URL <http://www.ncbi.nlm.nih.gov/pubmed/24556873>.

David Sarrut, Manuel Bardiès, Nicolas Boussion, Nicolas Freud, Sébastien Jan, Jean-Michel Létang, George Loudos, Lydia Maigne, Sara Marcatili, Thibault Mauxion, Panagiotis Papadimitroulas, Yann Perrot, Uwe Pietrzyk, Charlotte Robert, Dennis R Schaart, Dimitris Visvikis, and Irène Buvat. A review of the use and potential of the GATE Monte Carlo simulation code for radiation therapy and dosimetry applications. *Medical Physics*, 41(6), 2014. doi: <http://dx.doi.org/10.1118/1.4871617>. URL <http://scitation.aip.org/content/aapm/journal/medphys/41/6/10.1118/1.4871617>.

J Smeets, F Roellinghoff, D Prieels, F Stichelbaut, A Benilov, P Busca, C Fiorini, R Peloso, M Basilavichia, T Frizzi, J C Dehaes, and A Dubus. Prompt gamma imaging with a slit camera for real-time range control in proton therapy. *Physics in medicine and biology*, 57(11):3371–405, 2012. ISSN 1361-6560. doi: 10.1088/0031-9155/57/11/3371. URL <http://www.ncbi.nlm.nih.gov/pubmed/22572603>.

E Sterpin, G Janssens, J Smeets, François Vander Stappen, D Prieels, Marlen Priegnitz, Irene Perali, and S Vynckier. Analytical computation of prompt gamma ray emission and detection for proton range verification. *Physics in Medicine and Biology*, 60(12):4915–4946, 2015. ISSN 0031-9155. doi: 10.1088/0031-9155/60/12/4915. URL <http://stacks.iop.org/0031-9155/60/i=12/a=4915?key=crossref.aabd8815e135401a22d165e343a7bac4>.

E. Testa, M. Bajard, M. Chevallier, D. Dauvergne, F. Le Foulher, N. Freud, J. M. Letang, J. C. Poizat, C. Ray, and M. Testa. Monitoring the Bragg peak location of 73 MeV carbon ions by means of prompt  $\gamma$ -ray measurements. *Applied Physics Letters*, 93(9):1–10, 2008. ISSN 00036951. doi: 10.1063/1.2975841. URL <http://arxiv.org/abs/0809.0185><http://dx.doi.org/10.1063/1.2975841>.